

PRIMUS: GALAXY ENVIRONMENT ON THE QUIESCENT FRACTION EVOLUTION AT $Z < 1$

CHANGHOON HAHN, MICHAEL BLANTON, ALISON COIL, RICHARD COOL, DANIEL EISENSTEIN, JOHN MOUSTAKAS, KEN WONG, GUANGTUN ZHU
Draft version July 10, 2014

ABSTRACT

We investigate the effects of galaxy environment on the evolution of the quiescent fraction (f_Q) from $z = 0.8$ to 0.0 using spectroscopic redshifts and multi-wavelength imaging data from PRISM Multi-object Survey (PRIMUS) and the Sloan Digital Sky Survey (SDSS). Our stellar mass limited galaxy sample consists of ~ 40000 PRIMUS galaxies within $z = 0.2 - 0.8$ and ~ 130000 SDSS galaxies within $z = 0.0375 - 0.145$. We classify the galaxies as quiescent or star-forming, based on an evolving specific star formation cut, and as low or high density environments, based on fixed cylindrical aperture environment measurements on a volume-limited *Environment Definition Population* (from PRIMUS and SDSS). For each of these subsamples, we examine the stellar mass function (SMF) evolution and compute the $f_Q(\mathcal{M}_*)$. We find that in both low and high density environments the quiescent fraction increases with cosmic time over the probed redshift range. Moreover, the difference between the quiescent fraction in low and high density environments remains constant throughout the redshift range. These results suggest that the evolution of the quiescent fraction is independent of environment and provide constraints on quenching mechanisms in high density environments such as groups and clusters.

1. INTRODUCTION

Galaxies, in their detailed properties, carry the imprints of their surroundings, with a strong dependence of the quiescent fraction of galaxies on their local environment (e.g. Hubble 1936; Oemler 1974; Dressler 1980; Hermit et al. 1996; Guzzo et al. 1997; for a recent review see Blanton & Moustakas 2009). The strength of this dependence is itself a strongly decreasing function of galaxy stellar mass; at the extreme, the lowest masses ($< 10^9 M_\odot$) galaxies are quenched only in dense regions, and never in isolation (Geha et al. 2012). These effects vary with redshift at least in the densest clusters, as observed in the changing fraction of late-type spirals relative to the field found in studies of the morphology-density relation (Dressler 1984; Desai et al. 2007). Clearly understanding the properties of galaxies in the present-day universe requires a careful investigation of the role of environment, and how that role changes over time.

Nevertheless, the evolution of the role of environment is a relatively subtle effect and difficult to study. Although history of galaxies prior to $z \sim 1$ appears to have been one of rapid assembly, since that time the galaxy population has continued to evolve, but less dramatically. Although there are detectable changes in the population, the major classes of galaxies existed at $z \sim 1$, in roughly the same relative numbers as today (Bundy et al. 2006; Borch et al. 2006; Taylor et al. 2009; Moustakas et al. 2013a). Furthermore, at those redshifts we can also detect the dependence of galaxy properties on environment, with lower star-formation rate early-type galaxies populating the denser regions (Cooper et al. 2008; Patel et al. 2009; Kovač et al. 2010).

The most dramatic change in galaxy properties during the past eight billion years has been a remarkable decline in the star-formation rate of galaxies in the Universe (Hopkins & Beacom 2006). This decline appears dominated by decreases in the rates of star-formation of

individual galaxies (Noeske et al. (2007)). There is evidence that a large fraction of the decline associated with strongly infrared-emitting starbursts (Bell et al. 2005; Magnelli et al. 2009). The decline does not appear to be due to the quenching of a large fractions of the star-forming population, as reflected in observations of the stellar mass function of quiescent and star-forming galaxies (Blanton et al. (2006), Bundy et al. 2006; Borch et al. 2006; Moustakas et al. 2013a). These findings leave little room for the participation of environmentally-driven quenching in the global census of star-formation. As Cooper et al. (2008) and others have pointed out, because the environmental dependence of total star-formation rates at fixed redshift is relatively small, environmentally effects are unlikely to cause the overall star-formation rate decline.

Thus, the impact of environment on galaxy formation has to be interpreted on top of the background of this overall decline affecting galaxies in all environments. The most straightforward investigation of would directly determine the star-forming properties of galaxies as a function of environment, stellar mass and redshift in a single, consistently analyzed data set. This analysis can reveal how galaxies are quenched in the universe over time, quantitatively establish the contribution of environmental effects to the overall trends, and reveal whether those trends happen equally in all environments. However, such an analysis has not been done previously due to the lack of sufficiently large samples. In this paper, we apply this approach using the Prism Multi-object Survey (PRIMUS; Coil et al. (2011), Cool et al. (2013)), the largest available redshift survey covering the epochs between $0 < z < 1$.

In Section 2 we present a brief description of the PRIMUS and SDSS data, our sample construction, and galaxy environment measurements. In Section 3 we examine the stellar mass function evolution for star-forming/quiescent and high/low density environment

subsamples. In Section 4 compare the quiescent fraction evolution in high and low density environments. In Section 5 we summarize our results and discuss implications of the results on quenching mechanisms.

Throughout the paper we assume cosmology with $\Omega_m = 0.3$, $\Omega_\Lambda = 0.7$, and $H_0 = 70 \text{ km s}^{-1} \text{ Mpc}^{-1}$.

2. SAMPLE SELECTION

We are interested in quantifying the effects of galaxy environment on the evolution of the quiescent fraction over the redshift range $z < 1.0$. For our analysis, we require a sample with sufficient depth to probe the redshift range and robust redshifts to measure galaxy environment. PRIMUS, with its $\sim 120,000$ spectroscopic redshifts provides ideal data at intermediate redshifts for our analysis. In addition, we anchor our analysis of the intermediate redshift sample with a low redshift sample derived from SDSS.

In Section 2.1 and Section 2.2 we provide a brief summary of the PRIMUS data and the SDSS data used for our sample selection. Then in Section 2.3 we define our stellar mass complete galaxy sample. Afterwards, in Section 2.4, we classify our sample galaxies as quiescent or star-forming then calculate the environment using a volume-limited *Environment Defining Population* in Section 2.5. Finally in Section 2.6, we correct our galaxy sample and environment measurements for edge effects of the surveys.

2.1. PRIMUS

For our sample at intermediate redshifts we use multiwavelength imaging and spectroscopic redshifts from PRIMUS, a faint galaxy survey with $\sim 120,000$ precise spectroscopic redshifts ($\sigma_z/(1+z) \approx 0.5\%$) within the range $z \approx 0 - 1.2$. The survey was conducted using a IMACS spectrograph on a Magellan I Baade 6.5 m telescope with a slitmask and low dispersion prism. For details on the PRIMUS observation methods such as survey design, targeting, and data summary, we refer readers to the survey papers: Coil et al. (2011) and Cool et al. (2013).

While the PRIMUS survey targeted seven distinct extragalactic deep fields for a total of $\sim 9 \text{ deg}^2$, we restrict our sample to five fields that have *GALEX* and *Spitzer*/IRAC imaging (similar to the sample selection in Moustakas et al. (2013b)). Four of these fields are a part of the *Spitzer* Wide-area Infrared Extragalactic Survey (SWIRE¹): the European Large Area ISO Survey - South 1 field (ELAIS-S1²), the Chandra Deep Field South SWIRE field (CDFS), and the XMM Large Scale Structure Survey field (XMM-LSS). The XMM-LSS consists of two separate but spatially adjacent fields: the Subaru/XMM-Newton DEEP Survey field (XMM-SXDSS³) and the Canadian-France-Hawaii Telescope Legacy Survey field (XMM-CFHTLS⁴). Our fifth and final field is the Cosmic Evolution Survey (COSMOS⁵) field. For all of our fields we have near-UV

TABLE 1
GALAXY SUBSAMPLES

	z	Environment	Quiescent	Star-forming
SDSS	0.0375 – 0.145	High	5470	4501
		Low	5419	8927
PRIMUS	0.2 – 0.4	High	322	583
		Low	768	2516
PRIMUS	0.4 – 0.6	High	350	675
		Low	871	2385
PRIMUS	0.6 – 0.8	High	347	430
		Low	833	1847
PRIMUS	0.8 – 1.0	High	136	232
		Low	373	810

(NUV) and far-UV (FUV) photometry from the *GALEX* Deep Imaging Survey (DIS; Martin et al. (2005); Morrissey et al. (2005)) as well as ground-based optical and *Spitzer*/IRAC mid-infrared photometric catalogs. Moustakas et al. (2013b) provides detailed descriptions of integrated flux calculations in the photometric bands for each of our fields.

Finally, from the spectroscopic redshift and broad wavelength photometry we use *iSEDfit*, a Bayesian SED modeling code, to calculate stellar masses and star formation rates (SFRs) for our sample galaxies. *iSEDfit* uses the redshift and the observed photometry of the galaxies to determine the statistical likelihood of a large ensemble of generated model SEDs. The model SEDs are generated using Flexible Stellar Population Synthesis (FSPS) models (Conroy & Gunn (2010)) based on Chabrier (2003) IMF, along with other prior parameters beyond the scope of this paper. For details we refer readers to Section 4.1 and Appendix A. of Moustakas et al. (2013b). For the observed photometry, we use the *GALEX* FUV and NUV, the two shortest IRAC bands at 3.6 and 4.5 μm (the two longer-wavelength IRAC channels are excluded because *iSEDfit* does not model hot dust or polycyclic aromatic hydrocarbons emission lines), and the optical bands.

2.2. SDSS-GALEX

For our low redshift sample, we use spectroscopic redshifts and high fidelity *ugriz* photometry from the SDSS Data Release 7 (DR7; Abazajian et al. (2009)). More specifically we select galaxies from the New York University Value-Added Galaxy Catalog (SDSS VAGC) that satisfy the main sample criterion and have galaxy extinction corrected Petrosian magnitudes $14.5 < r < 17.6$ and spectroscopic redshifts within $0.01 < z < 0.2$ (Blanton et al. (2005)). We further narrow down the SDSS VAGC sample to only galaxies with medium depth observations with total exposure time greater than 1 ks from *GALEX* Release 6. This SDSS-*GALEX* sample contains 167,727 galaxies.

Using the MAST/CasJobs⁶ interface and a 4'' diame-

¹ <http://swire.ipac.caltech.edu/swire/swire.html>

² <http://dipastro.pd.astro.it/esis>

³ <http://www.naoj.org/cience/SubaruProject/SDS>

⁴ <http://www.cfht.hawaii.edu/Science/CFHLS>

⁵ <http://cosmos.astro.caltech.edu>

⁶ <http://galex.stsci.edu/casjobs>

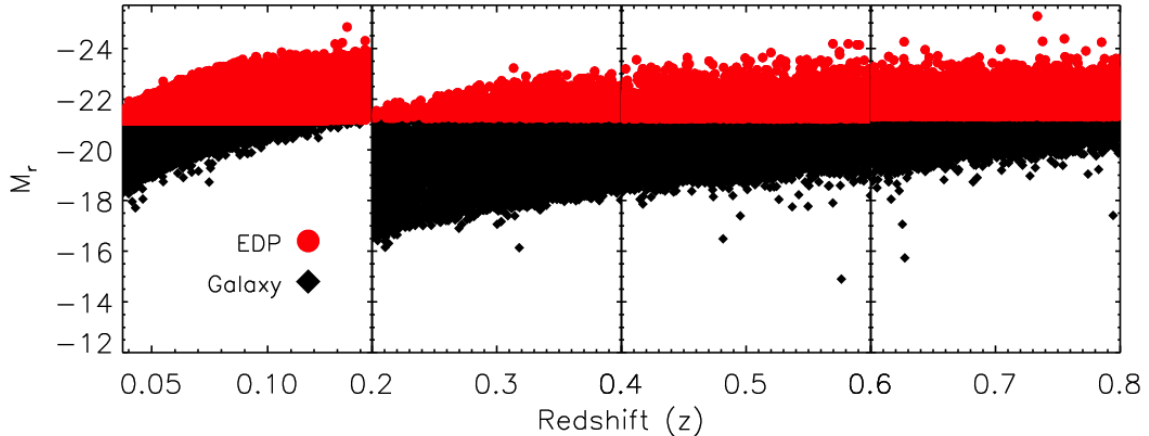


FIG. 1.— Absolute magnitude M_r versus redshift for the target galaxy population (black squares) with the Environment Defining Population (red circles) plotted on top. Both samples are divided into redshift bins: $z \approx 0.0375 - 0.145$, $0.2 - 0.4$, $0.4 - 0.6$, and $0.6 - 0.8$ (panels left to right). Stellar mass completeness limits are imposed on the target galaxy population (Section 2.3) while the M_r limits are imposed on the EDP (Section 2.5). The lowest redshift bin ($z \approx 0.0375 - 0.145$; leftmost panel) contain our galaxy sample and EDP selected from SDSS. The rest contain galaxies and EDP selected from PRIMUS.

ter search radius, we obtain the NUV and FNU photometry for the SDSS-*GALEX* galaxies. For optical photometry, we use the *ugriz* bands from the SDSS model magnitudes scaled to the *r*-band *cmodel* magnitude. These photometric bands are then supplemented with integrated *JHK_s* magnitudes from the 2MASS Extended Source Catalog (XSC; Jarrett et al. (2000)) and with photometry at 3.4 and 4.6 μm from the WISE All-Sky Data Release⁷. Further details regarding the SDSS-*GALEX* sample photometry can be found in Section 2.4 of Moustakas et al. (2013b). As we did with the PRIMUS data above, we use *iSEDfit* with the above observed photometry to obtain the stellar masses and star formation rates for the SDSS-*GALEX* sample.

While the SDSS-*GALEX* data discussed above is derived from SDSS VAGC Data Release 7, since the release of the catalog, there have been significant improvements in the photometry. Notably, Blanton et al. (2011) find that the background subtractions in SDSS Data Release 7 has a size dependent bias in the galaxy fluxes, where galaxy fluxes are underestimated by ~ 1.5 mag for galaxies with $r_{50} \sim 100$ arcsec. In addition Bernardi et al. (2013) find that the luminosity, and ultimately stellar mass, is underestimated when they are derived from the SDSS *cmodel* magnitudes in comparison to *PyMorph* single-Sersic and Sersic-Exponential fits to the surface brightness profiles.

In order to quantify the effects of these photometric underestimations in our analysis, we replace our SDSS fluxes in the *ugriz* band with *ugriz* fluxes from the NASA-Sloan Atlas (NSA) catalog, which incorporate the background subtraction improvements presented in Blanton et al. (2011) and are single-Sersic fit fluxes rather than the standard SDSS *cmodel* fluxes. Using the ratio of the luminosity derived from the improved photometry over the luminosity derived from the standard SDSS VAGC photometry, we impose a correction on the stellar mass values obtained from *iSEDfit* assuming a

constant mass-to-light ratio. This mass correction leads to a significant increase in the stellar mass function for $\mathcal{M} > 10^{11} \mathcal{M}_\odot$ that matches the results from Bernardi et al. (2013). However, the effect of the mass correction was negligible for the quiescent fraction evolution results. As a result, we do not discuss the issues with photometric measurements any further in this paper. The effects of the discussed photometry methods on the luminosity function and stellar mass function will be examined in detail in future work.

2.3. Galaxy Sample

Using the low redshift SDSS-*GALEX* and intermediate redshift PRIMUS data described above, in this section, we define our galaxy sample which will be used to compute the SMFs and QFs. For PRIMUS, we begin with the selection criteria imposed in Moustakas et al. (2013b) for their parent sample. We take the statistically complete *primary* sample from the PRIMUS data (Coil et al. (2011)) and impose magnitude limits on optical selection bands as specified in Moustakas et al. (2013b) Table 1. These limits are in different optical selection bands and have distinct values for the five PRIMUS target fields. We then exclude stars and broad-line AGN to only select objects spectroscopically classified as galaxies, with high-quality spectroscopic redshifts ($Q \geq 3$). In addition we impose a redshift range of $0.2 < z < 0.8$ for the PRIMUS galaxy sample, where $z > 0.2$ is selected due to limitations from sample variance and $z < 0.8$ is selected due to the lack of sufficient statistics in subsamples defined below.

For the PRIMUS objects that meet the above criteria, we assign statistical weights (described in Coil et al. (2011) and Coil et al. (2013)) in order to correct for targeting incompleteness and redshift failures. The statistical weight, w_i , for each galaxy is given by

$$w_i = (f_{\text{target}} \times f_{\text{collision}} \times f_{\text{success}})^{-1}, \quad (1)$$

Equation (1) in Moustakas et al. (2013b). Given that our ultimate interest is in deriving the SMFs and QFs

⁷ <http://wise2.ipac.caltech.edu/docs/release/allsky>

from our sample, we impose stellar mass limits in order to derive a stellar mass complete galaxy sample.

Stellar mass completeness limits for a magnitude-limited survey such as PRIMUS is a function of redshift, the apparent magnitude limit of the survey, and the typical stellar mass-to-light ratio of galaxies near the flux limit. As done in Moustakas et al. (2013b), we follow Pozzetti et al. (2010) to empirically determine the stellar mass completeness limits. For each of the target galaxies we compute \mathcal{M}_{lim} using $\log \mathcal{M}_{\text{lim}} = \log \mathcal{M} + 0.4(m - m_{\text{lim}})$, where \mathcal{M} is the stellar mass of the galaxy in \mathcal{M}_{\odot} , \mathcal{M}_{lim} is the stellar mass of each galaxy if its magnitude was equal to the survey magnitude limit, m is observed apparent magnitude in the selection band, and m_{lim} is the magnitude limit for our five fields mentioned above. We construct a cumulative distribution of \mathcal{M}_{lim} for the 15% faintest galaxies in $\Delta z = 0.04$ bins. In each of these redshift bins, we calculate the minimum stellar mass that includes 95% of the galaxies. Separately for quiescent and star-forming galaxies, we fit quadratic polynomials to the minimum stellar masses versus redshift (galaxies are classified into star-forming or quiescent in the following section). Finally, we use the polynomials to obtain the minimum stellar masses at the center of redshift bins, $0.2 - 0.4$, $0.4 - 0.6$, and $0.6 - 0.8$, which are then used as PRIMUS stellar mass completeness limits.

To derive the low redshift portion of our galaxy sample, we start by limiting the SDSS-*GALEX* data to objects within $0.0375 < z < 0.145$, a redshift range later imposed on the volume-limited Environment Defining Population (Section 2.5). To account for the targeting incompleteness of the SDSS-*GALEX* sample, we use the statistical weight estimates provided by the NYU-VAGC catalog. Furthermore, to derive a stellar mass complete sample, we impose a uniform stellar mass limit of $10^{9.8} \mathcal{M}_{\odot}$, which is determined from the mass-to-light ratio completeness limit of the SDSS-*GALEX* sample within the imposed redshift limit.

With the stellar mass completeness limits above, we have a stellar mass complete sample derived from SDSS-*GALEX* and PRIMUS. However since our sample is derived from two different surveys, we must account for the disparity in the redshift uncertainty. While PRIMUS provides precise spectroscopic redshifts with $\sigma_z/(1+z) \approx 0.5\%$, due to the higher redshift ranges it probes the uncertainties are significantly greater than that of the SDSS-*GALEX* redshifts. The differences in redshift uncertainties becomes especially important in environment classifications (environment measurements and classification is later discussed in Section 2.5). In order to have comparable contamination in environment classifications, we apply PRIMUS redshift uncertainties to our galaxy sample selected from SDSS-*GALEX*. For each SDSS-*GALEX* galaxy in our sample, we compute its σ_z by randomly sampling within three standard deviations of a normal distribution where the standard deviation is derived from the $z_{\text{SDSS-GALEX}}$ of the galaxy, $\sigma = 0.005(1 + z_{\text{SDSS-GALEX}})$.

The absolute magnitude (M_r) versus redshift for the galaxy sample (black squares) is plotted in Figure 1. The left-most panel corresponds to the portion of the sample derived from the SDSS-*GALEX* data and the rest correspond to the target sample derived from the PRIMUS data divided in bins with $\Delta z \sim 0.2$.

2.4. Classifying Quiescent and Star-Forming Galaxies

With the galaxy sample defined in the previous section, we now classify the galaxies as quiescent or star-forming using an evolving cut based on specific star-formation rate utilized in Moustakas et al. (2013b) Section 3.2. This classification method utilizes the star-forming (SF) sequence, which is the correlation between star-formation rate (SFR) and stellar mass in star-forming galaxies observed at least until $z \sim 2$ (Noeske et al. (2007)). The PRIMUS sample displays a well-defined SF sequence within the redshift range of our galaxy sample. Then using the power-law slope for the SF sequence derived by Salim et al. (2007) ($\text{SFR} \propto \mathcal{M}^{0.65}$) and the minimum of the quiescent/star-forming bimodality, determined empirically, we obtain the following equation to classify the target galaxies (Equation 2 in Moustakas et al. (2013b)):

$$\log(\text{SFR}_{\text{min}}) = -0.49 + 0.64 \log(\mathcal{M} - 10) + 1.07(z - 0.1), \quad (2)$$

where \mathcal{M} is the stellar mass of the galaxy. If the target galaxy SFR and stellar mass lies above Equation 2.4 we classify it as star-forming; if below, as quiescent (Moustakas et al. (2013b) Figure 1.).

2.5. Galaxy Environment

With the galaxy sample divided into quiescent and star-forming galaxies above, we now classify the galaxies into high and low density environments. In this section, we describe our method for measuring the environment for our galaxy sample. First, we define the environment of a galaxy as the number of neighboring *Environment Defining Population* galaxies (defined below) within a fixed aperture centered around it. We use a fixed aperture measurement of environment because, as Muldrew et al. (2012) finds in their comparison of different environment definition using simulations, it provides a better probe of the entire halo in comparison to other definitions of environment such as nearest neighbor, which provides a better tracer at inter-halo scales. For our aperture, we use a cylinder of dimensions: $R_{\text{ap}} = 2$ Mpc/h and $H_{\text{ap}} = 25$ Mpc/h. Though spherical apertures are often used in literature (e.g. Croton et al. (2005)), we use a cylindrical aperture in order to account for the PRIMUS redshift errors and redshift space distortions (i.e. "Finger of God" effect). Cooper et al. (2005) finds that $\pm 1000 \text{ km s}^{-1}$ optimally reduces the effects of redshift space distortions and the PRIMUS redshift uncertainty at $z \sim 0.7$ corresponds to $\sigma_z < 0.01$, so aperture height of 25 Mpc/h accounts for both of these effects. Our choice of cylinder radius was motivated by scale dependence analyses in literature (Blanton et al. (2006), Wilman et al. (2010), and Muldrew et al. (2012)), which suggest that galactic properties such as color and quenched fractions are dependent on halo-scale properties such as host dark matter halo mass. Wilman et al. (2010), which uses environment defined by annuli of different radii, find positive correlation for quenched fraction and color on scales < 1 Mpc and anti-correlation on scales > 3 Mpc. Our choice of 2Mpc/h provides sufficient sample size of galaxies in dense environments, for robust statistics, while tracing galactic properties within the halo scale. When we extend our analysis to cylindrical apertures with $R_{\text{ap}} = 1$ Mpc/h, we find that the

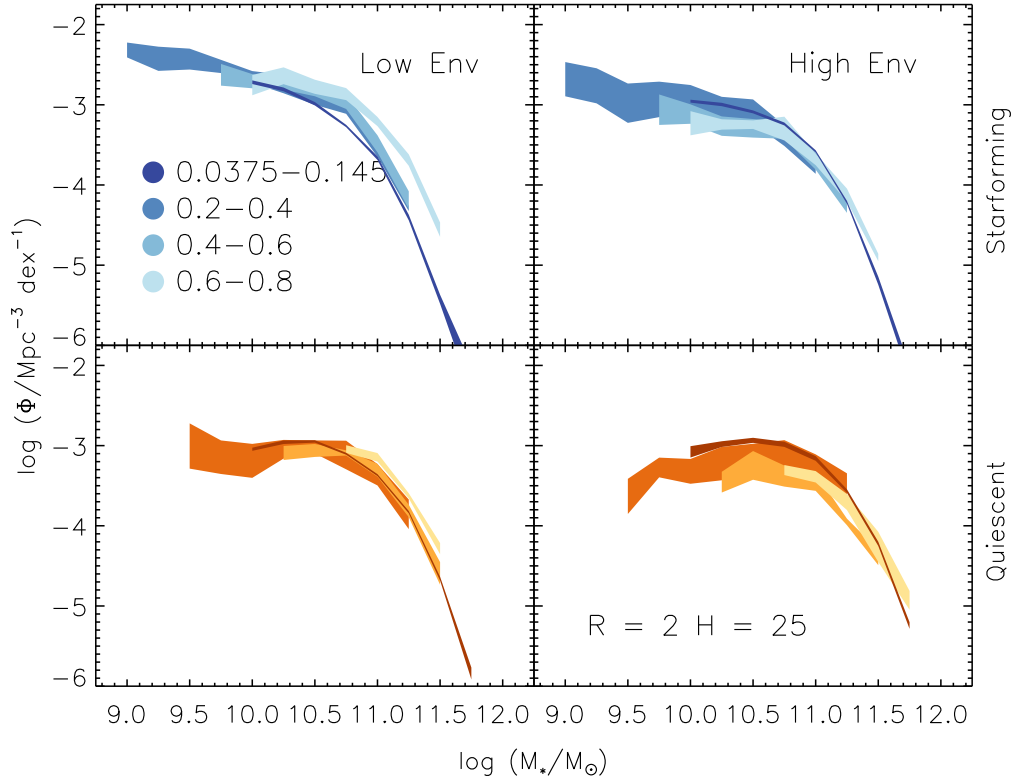


FIG. 2.— Evolution of stellar mass functions of star-forming (top) and quiescent (bottom) target galaxies in low (left) and high (right) environments from redshift range $z = 0 - 0.8$. The environment of each galaxy was calculated using a cylindrical aperture size of $R = 2$ Mpc and $H = 25$ Mpc and classification based on the cut-offs specified in Table 2. The SMFs use mass bins of width $\Delta \log(M/M_\odot) = 0.25$. In each panel we use shades of blue (star-forming) and orange (quiescent) to represent the SMF at different redshift, higher redshifts being progressively lighter.

change does not qualitatively change our results (difference in $f_Q < 0.05$).

Using the fixed aperture environment definition, we now measure the environment for our galaxy sample. First, we construct a volume limited *Environment Defining Population* (EDP) with absolute magnitude cut-offs (M_r) at redshift bin of $\Delta z \sim 0.2$. The M_r cut-offs for the EDP are selected such that the cumulative number density over M_r for all redshift bins are equal. In addition to providing a reasonable comparison of environment measurements for wide redshift range, it also seeks to construct an EDP that contains similar galaxy populations through the redshift range (i.e. accounts for the progenitor bias). As Behroozi et al. (2013) and Leja et al. (2013) find in their analysis of the cumulative number density method, though it does not precisely account for the scatter in mass accretion or galaxy-galaxy mergers, it provides a reasonable means to compare galaxy populations over a wide range of cosmic time.

In constructing the EDP for the PRIMUS (hereafter PRIMUS EDP) we use the same PRIMUS data used to select our galaxy sample (described in Section 2.3). We restrict the PRIMUS galaxies to $0.2 < z < 0.8$ and divide them into bins of $\Delta z = 0.2$. Before we consider the cumulative number densities in these bins, we first determine the M_r limit for the highest redshift bin ($0.6 - 0.8$) by examining the M_r distribution with bin size $\Delta M_r = 0.25$ and select $M_{r,\text{lim}}$ near the peak

of the distribution where bins with $M_r > M_{r,\text{lim}}$ have fewer galaxies than the bin at $M_{r,\text{lim}}$. We conservatively choose $M_{r,\text{lim}}(0.6 < z < 0.8)$ to be $M_r = -20.75$. Then for the lower redshift bins, we impose absolute magnitude limits ($M_{r,\text{lim}}$) such that the cumulative number density of the bin ordered by M_r is equal to the cumulative number density of the highest redshift bin at $M_{r,\text{lim}}(0.6 < z < 0.8) = -20.75$. In these cumulative number density calculations, we account for the statistical weights of the galaxies (Section 2.1 and 2.2).

For the EDP of the SDSS-*GALEX* galaxy sample (hereafter SDSS EDP), we do not use the SDSS-*GALEX* parent data which uses the geometry of the combined angular selection function of the SDSS VAGC and *GALEX* (Section 2.2). Instead, since FUV, NUV values are not necessary for EDP, we extend the parent data of the SDSS EDP to the entire SDSS VAGC, including galaxies outside of the *GALEX* window function. Furthermore, we impose a redshift range of $0.0375 - 0.145$ on the SDSS EDP. This redshift range was empirically determined to account for the lack of faint galaxies at $z \sim 0.2$ and the lack of bright galaxies at $z \sim 0.01$ in the SDSS VAGC. The lower bound was determined by the bright limit and the upper bound by the faint limit of the M_r versus redshift distribution. As with the PRIMUS redshift bins, we determine the SDSS EDP $M_{r,\text{lim}}$ by matching the cumulative number density of the highest redshift bin. We get $M_{r,\text{lim}} = -20.57, -20.73, -20.80$ and -20.95 for the

redshift bins $0.0375 - 0.145$, $0.2 - 0.4$, $0.4 - 0.6$, $0.6 - 0.8$, respectively. These absolute magnitude limits are illustrated in Figure 1, which show clear M_r cutoffs in the M_r distribution versus redshift for the EDP (red circles) on top of the target galaxy sample (black).

Finally we measure the environment for each galaxy in our sampling by counting the number of EDP galaxies, n_{env} with RA , Dec , and z within our cylindrical aperture centered around it. Note that n_{env} accounts for the statistical weights of the EDP galaxies. Once we obtain environment measurements for all the galaxies in our galaxy sample, we classify galaxies with $n_{\text{env}} < 1$ to be "low" environment density and galaxies with $n_{\text{env}} > 3$ to be "high" environment densities. The high environment cutoff was selected in order to reduce contamination from galaxies in low environment densities while maintaining sufficient

2.6. Edge Effects

One of the challenges in obtaining accurate galaxy environments using a fixed aperture method is accounting for the edges of the survey. For galaxies located near the edge of the survey, part of the fixed aperture encompassing it will lie outside the survey regions. In this case, n_{env} only reflects the fraction of the environment within the survey geometry.

To account for these edge effects, we use a Monte Carlo method to impose edge cutoffs on our galaxy sample. We begin by computing the angular separation, θ_{ap} that corresponds to the radius of the fixed aperture (used to measure environment) at the redshifts of the galaxies. Then we compute the environment, n_{ransack} , of our galaxy sample with the EDP replaced by a ransack sample of $N_{\text{ransack}} = 1,000,000$ points with RA and Dec randomly selected within the window function of the EDP. We compare the n_{ransack} values to the expected value computed based on the angular area of the environment defining aperture and the EDP window function:

$$E[n_{\text{ransack}}] = \frac{N_{\text{ransack}}}{A_{\text{EDP}}} \times \pi \theta_{\text{ap}}^2 \times f_{\text{thresh}}. \quad (3)$$

A_{EDP} is the total angular area of the EDP window function and f_{thresh} is the fractional threshold for the edge effect cut-off, which we vary based on R_{ap} (listed in Table 2). If n_{ransack} for a target galaxy is greater than $E[n_{\text{ransack}}]$ then the galaxy remains in our sample; otherwise, it is discarded.

3. STELLAR MASS FUNCTION

The target galaxy sample defined above has so far been classified into quiescent or star-forming and low or high density environments. We further divide these subsamples into bins of redshift: $0.0375 - 0.145$, $0.2 - 0.4$, $0.4 - 0.6$, and $0.6 - 0.8$ for a total 16 subsamples. In this section, we calculate the SMF for each of these 16 subsamples.

To calculate the SMFs we employ a non-parametric $1/V_{\text{max}}$ estimator commonly used for galaxy luminosity functions and stellar mass functions, as done in Moustakas et al. (2013b) and discussed in the review Johnston (2011). The differential SMF is given by the following

equation:

$$\Phi(\log \mathcal{M}) \Delta(\log \mathcal{M}) = \sum_{i=1}^N \frac{w_i}{V_{\text{max,avail},i}}. \quad (4)$$

The equation above is same as Equation 3. in Moustakas et al. (2013b) except for $V_{\text{max,avail}}$ instead than V_{max} , to account for the edge effects of the survey discussed in Section 2.6. w_i is the statistical weight of galaxy i and $\Phi(\log \mathcal{M}) \Delta(\log \mathcal{M})$ is the number of galaxies (N) per unit volume within the stellar mass range $[\log \mathcal{M}, \log \mathcal{M} + \Delta(\log \mathcal{M})]$.

$V_{\text{max},i}$ is the maximum cosmological volume where it is possible to observe galaxy i given the apparent magnitude limits of the survey. However in Section 2.6 we remove galaxies that lie on the edge from our sample. In doing so we reduce the maximum cosmological volume where a galaxy can be observed, thereby reducing $V_{\text{max},i}$. We introduce the term $V_{\text{max,avail},i}$ for the $V_{\text{max},i}$ value that accounts for the survey edge effects.

To calculate $V_{\text{max,avail},i}$, we generate a sample of points with random RA , Dec within the window function of our galaxy sample (SDSS-*GALEX* window function and the five PRIMUS fields) and random z within the redshift range. This is not to be confused with the ransack sample in Section 2.6. We then impose the same edge effect cutoffs we applied to our galaxy sample, using the same ransack environment calculation method from above. At redshift bins of $\Delta z \sim 0.01$, we compute the fraction of random points that remain in the bin after the edge effect cutoffs: f_{edge} . We then apply this factor to compute $V_{\text{max,avail}} = V_{\text{max}} \times f_{\text{edge}}$. The V_{max} in the equation above are computed following the method described in Moustakas et al. (2013b) Section 4.2 with the same redshift-dependent K -correction from observed SED and luminosity evolution model.

In order to calculate the uncertainty of the SMFs from the sample variance, we use a standard jackknife technique (as done in Moustakas et al. (2013b)). For the PRIMUS galaxies, we calculate SMFs after excluding one of the five target fields at a time. For the SDSS target galaxies we divide the field into a 12×9 rectangular RA and Dec grid and calculate the SMFs after excluding one grid each time. Then using the calculated SMFs we calculate the uncertainty:

$$\sigma^j = \sqrt{\frac{M-1}{M} \sum_{k=1}^M (\Phi_k^j - \langle \Phi^j \rangle)^2} \quad (5)$$

M in this equation is the number of jack knife SMFs in the stellar mass bin. $\langle \Phi^j \rangle$ is the mean number density of galaxies in each stellar mass bin for all of the jack knife Φ^j s.

We present the SMFs for 16 target galaxy subsamples classified into quiescent/star-forming (orange/blue, bottom/top panels) and high/low environment density (left/right panels) in Figure 2. The redshift evolution of the SMFs in each of these panels are indicated by a darker shade for lower redshift bins. The sample variance uncertainties are incorporated in the width of the SMFs.

Examining the SMF evolution from $z \sim 0.7$ to $z \sim 0.1$, we find that in high density environments both the star-

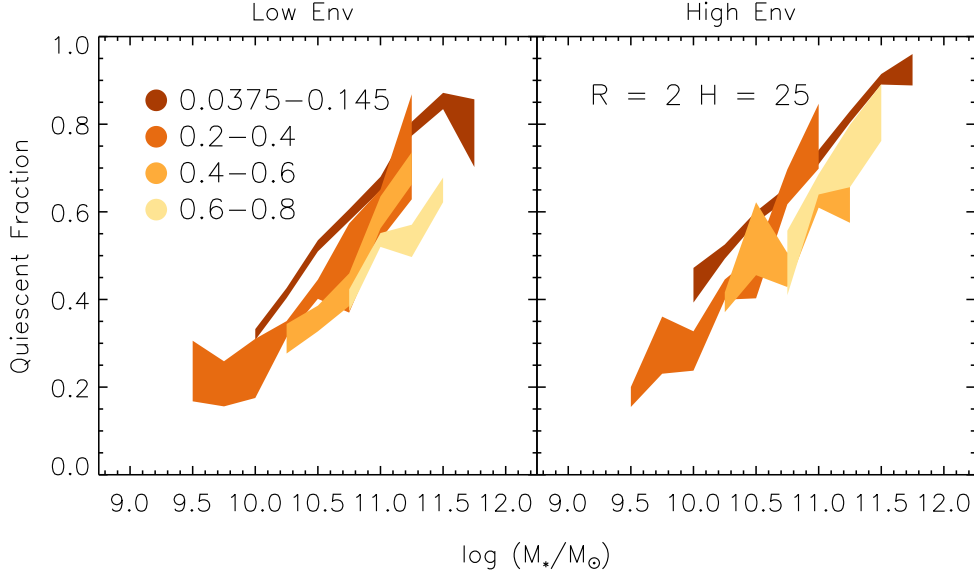


FIG. 3.— Evolution of the quiescent fraction f_Q for galaxies in low (left) and high (right) density environments for $z < 0.8$. f_Q s were calculated using the SMFs in Figure 2, as described in text. Darker shading indicates lower redshift.

forming and quiescent SMFs increase at \mathcal{M}_* below the knee of mass function ($\log \mathcal{M}_*/\mathcal{M}_\odot < 10.75$ for star-forming; $\log \mathcal{M}_*/\mathcal{M}_\odot < 11.0$ for quiescent). Meanwhile, at masses above the knee the SMFs for high density environments exhibit little change over the entire cosmic time range.

At low density environments, the quiescent SMF remains relatively constant for galaxies with $\log \mathcal{M}_*/\mathcal{M}_\odot < 10.75$. At higher stellar masses, however, the quiescent low density environment SMF decreases notably. Finally, the low density environment star-forming SMF shows a decrease at all stellar mass ranges over the redshift range. We caution readers and reserve any detailed analysis of the SMF evolution to future work due to the improvements in photometry that significantly alter the lowest redshift bin SMFs mentioned in Section 2.2.

4. QUIESCENT FRACTION

The SMFs calculated in the previous section describe the stellar mass distribution of our galaxy population and reveal the evolution of this distribution over cosmic time. When we compute the quiescent fractions we compare the quiescent and the star-forming populations and quantify the fraction of galaxies that have depleted their star-formation. By adding environment classifications to our analysis, we investigate the effects of the environment on the quiescent fraction and its evolution. Moreover, by analyzing the quiescent fraction, we are able to reveal the environment dependence of quenching mechanisms.

From the SMF number densities (Φ) the quiescent fraction is computed as follows,

$$f_Q = \frac{\Phi_Q}{\Phi_{SF} + \Phi_Q}. \quad (6)$$

Φ_Q and Φ_{SF} are the total number of galaxies per unit volume in stellar mass bin of $\Delta(\log \mathcal{M}) = 0.25$ for the quiescent and star-forming subsamples, respectively (Equation 4). We compute f_Q for high and low density en-

vironments for all redshift bins as plotted in Figure 3, which shows the evolution of f_Q for high (right) and low (left) density environments. As in Figure 2, the darker shading represent lower redshift bins.

In both high and low density environments, Figure 3 shows a clear increase in f_Q with decrease in redshift at all stellar masses. Qualitatively, this f_Q evolution exhibits a noticeable mass dependence. More specifically, the f_Q in low density environments shows a greater evolution between redshift bins at high masses than at low masses. On the other hand, the f_Q in high density environments shows a greater evolution between redshift bins at low masses than at high masses.

While Figure 3 show the apparent trends, quantitative comparisons of f_Q for different density environment over redshift is made challenging by the distinct stellar mass limits at each redshift bin. In order to quantify the quiescent fraction over the stellar mass complete rate, we fit each f_Q to a power-law parameterization as a function of stellar mass,

$$f_Q(\mathcal{M}_*) = a \log \left(\frac{\mathcal{M}_*}{10^{10.5} \mathcal{M}_\odot} \right) + b, \quad (7)$$

where a and b are best-fit parameters using *MPFIT* (Markwardt (2009)). The value $10^{10.5} \mathcal{M}_\odot$ in the equation represents an empirically selected fiducial mass \mathcal{M}_{fid} within the stellar mass limits where there is a sufficiently large number of galaxies. This fiducial mass serves to highlight and quantify the f_Q evolution for different redshifts and using $\mathcal{M}_{\text{fid}} = 10^{11} \mathcal{M}_\odot$ does not notably alter the results. Figure 4 shows the evolution of $f_Q(\mathcal{M}_{\text{fid}})$ from $z \sim 0.7$ to ~ 0.1 for low (diamond) and high (circle) density environments. For both density environments, $f_Q(\mathcal{M}_{\text{fid}})$ increases as redshift decreases similar to the trend we noted qualitatively. In addition, throughout the redshift range, high density environment $f_Q(\mathcal{M}_{\text{fid}})$ is significantly greater than the low density environment $f_Q(\mathcal{M}_{\text{fid}})$. However when we compute $f_Q(\mathcal{M}_{\text{fid}})_{\text{high}} - f_Q(\mathcal{M}_{\text{fid}})_{\text{low}}$, we find the difference

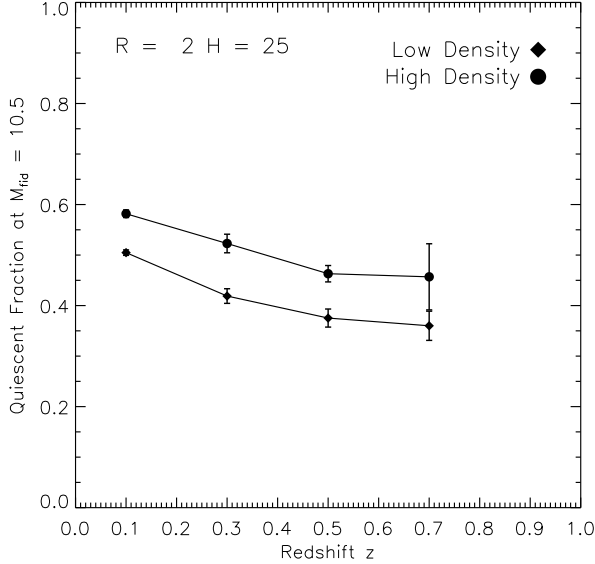


FIG. 4.— The evolution of the quiescent fraction at fiducial mass, $f_Q(\mathcal{M}_{\text{fid}} = 10^{10.5} \mathcal{M}_\odot)$, for low (square) and high (circle) density environments within the redshift range $z = 0.0 - 0.8$. There is a significant increase in $f_Q(\mathcal{M}_{\text{fid}})$ with decrease in redshift for both environments. In addition, over the entire redshift range, high density environment $f_Q(\mathcal{M}_{\text{fid}})$ is greater than low density environment $f_Q(\mathcal{M}_{\text{fid}})$. However the difference in $f_Q(\mathcal{M}_{\text{fid}})$ for the two environments remains constant throughout suggesting that while the quiescent fraction is higher in dense environments, the evolution of the quiescent fraction is independent of environment.

remains constant throughout the redshift range (< 0.15

throughout redshift range). Furthermore, the total evolution of $f_Q(\mathcal{M}_{\text{fid}})$ from $z \sim 0.7$ to ~ 0.1 show no strong environment dependence.

The analysis described in this paper use a fixed cylindrical aperture with dimensions $R_{\text{ap}} = 2$ Mpc and $H_{\text{ap}} = 25$ Mpc to measure environment, the same analysis was extended for varying aperture dimensions $R_{\text{ap}} = 1, 2, 3$ Mpc and $H_{\text{ap}} = 25, 50$ Mpc. Minor adjustments to the environment classification thresholds were adopted in these analyses for the smaller apertures ($r_{\text{ap}} = 0.5, 1$ Mpc and $r_{\text{ap}} = 25$ Mpc). The results obtained from using these different are consistent with the results displayed in this paper.

5. SUMMARY

Using a stellar mass complete galaxy sample, we demonstrate that the quiescent fraction increases over cosmic time for $z < 0.8$. Furthermore with a consistently measured galaxy environment from robust spectroscopic redshift, we demonstrate that the quiescent fraction in high density environments is always greater than the fraction in low density environments. While the difference in quiescent fraction between the two environments is significant, it remains constant throughout the redshift range suggesting that the evolution of the quiescent fraction is independent of environment.

• Comparison to other works.

- Alberts et al. 2013
- Tinker et al. 2011
- Geha et al. 2012

REFERENCES

- Abazajian, K. N., Adelman-McCarthy, J. K., Agüeros, M. A., et al. 2009, *ApJS*, 182, 543
- Behroozi, P. S., Marchesini, D., Wechsler, R. H., et al. 2013, *ApJ*, 777, L10
- Bell, E. F., Papovich, C., Wolf, C., et al. 2005, *ApJ*, 625, 23
- Bernardi, M., Meert, A., Sheth, R. K., et al. 2013, *MNRAS*, 436, 697
- Blanton, M. R., Eisenstein, D., Hogg, D. W., & Zehavi, I. 2006, *ApJ*, 645, 977
- Blanton, M. R., Kazin, E., Muna, D., Weaver, B. A., & Price-Whelan, A. 2011, *AJ*, 142, 31
- Blanton, M. R., & Moustakas, J. 2009, *ARA&A*, 47, 159
- Blanton, M. R., Schlegel, D. J., Strauss, M. A., et al. 2005, *AJ*, 129, 2562
- Borch, A., Meisenheimer, K., Bell, E. F., et al. 2006, *A&A*, 453, 869
- Bundy, K., Ellis, R. S., Conselice, C. J., et al. 2006, *ApJ*, 651, 120
- Chabrier, G. 2003, *PASP*, 115, 763
- Coil, A. L., Blanton, M. R., Burles, S. M., et al. 2011, *ApJ*, 741, 8
- Conroy, C., & Gunn, J. E. 2010, *FSPS: Flexible Stellar Population Synthesis*, astrophysics Source Code Library, ascl:1010.043
- Cool, R. J., Moustakas, J., Blanton, M. R., et al. 2013, *ApJ*, 767, 118
- Cooper, M. C., Newman, J. A., Madgwick, D. S., et al. 2005, *ApJ*, 634, 833
- Cooper, M. C., Newman, J. A., Weiner, B. J., et al. 2008, *MNRAS*, 383, 1058
- Croton, D. J., Farrar, G. R., Norberg, P., et al. 2005, *MNRAS*, 356, 1155
- Desai, V., Dalcanton, J. J., Aragón-Salamanca, A., et al. 2007, *ApJ*, 660, 1151
- Dressler, A. 1980, *ApJ*, 236, 351
- Dressler, A. 1984, *ARA&A*, 22, 185
- Geha, M., Blanton, M. R., Yan, R., & Tinker, J. L. 2012, *ApJ*, 757, 85
- Guzzo, L., Strauss, M. A., Fisher, K. B., Giovanelli, R., & Haynes, M. P. 1997, *ApJ*, 489, 37
- Hermis, S., Santiago, B. X., Lahav, O., et al. 1996, *MNRAS*, 283, 709
- Hopkins, A. M., & Beacom, J. F. 2006, *ApJ*, 651, 142
- Hubble, E. P. 1936, *The Realm of the Nebulae* (New Haven: Yale University Press)
- Jarrett, T. H., Chester, T., Cutri, R., et al. 2000, *AJ*, 119, 2498
- Johnston, R. 2011, *A&A Rev.*, 19, 41
- Kovač, K., Lilly, S. J., Knobel, C., et al. 2010, *ApJ*, 718, 86
- Leja, J., van Dokkum, P., & Franx, M. 2013, *ApJ*, 766, 33
- Magnelli, B., Elbaz, D., Chary, R. R., et al. 2009, *A&A*, 496, 57
- Markwardt, C. B. 2009, in *Astronomical Society of the Pacific Conference Series*, Vol. 411, *Astronomical Data Analysis Software and Systems XVIII*, ed. D. A. Bohlender, D. Durand, & P. Dowler, 251
- Martin, D. C., Fanson, J., Schiminovich, D., et al. 2005, *ApJ*, 619, L1
- Morrissey, P., Schiminovich, D., Barlow, T. A., et al. 2005, *ApJ*, 619, L7
- Moustakas, J., Coil, A. L., Aird, J., et al. 2013a, *ApJ*, 767, 50
- . 2013b, *ApJ*, 767, 50
- Muldrew, S. I., Croton, D. J., Skibba, R. A., et al. 2012, *MNRAS*, 419, 2670
- Noeske, K. G., Weiner, B. J., Faber, S. M., et al. 2007, *ApJ*, 660, L43
- Oemler, A. 1974, *ApJ*, 194, 1
- Patel, S. G., Holden, B. P., Kelson, D. D., Illingworth, G. D., & Franx, M. 2009, *ApJ*, 705, L67
- Pozzetti, L., Bolzonella, M., Zucca, E., et al. 2010, *A&A*, 523, A13
- Salim, S., Rich, R. M., Charlot, S., et al. 2007, *ApJS*, 173, 267

TABLE 2
ENVIRONMENT DEFINING APERTURE DIMENSIONS

Radius (Mpc)	Height (Mpc)	Edge Effect Cutoff	High Env (galaxies)	Low Env (galaxies)
1.0	50	80%	1.5	0.0
2.0	50	75%	4.0	0.0

Taylor, E. N., Franx, M., van Dokkum, P. G., et al. 2009, ApJ,
694, 1171
Wilman, D. J., Zibetti, S., & Budavári, T. 2010, MNRAS, 406,
1701

APPENDIX